

Cite this: *Chem. Sci.*, 2024, **15**, 10858

All publication charges for this article have been paid for by the Royal Society of Chemistry

## Enhancing local K<sup>+</sup> adsorption by high-density cube corners for efficient electroreduction of CO<sub>2</sub> to C<sub>2+</sub> products†

Hu Zang,<sup>a</sup> Changjiang Liu,<sup>a</sup> Qinyuan Ji,<sup>a</sup> Jiahao Wang,<sup>a</sup> Haiyan Lu,<sup>a</sup> Nan Yu<sup>a</sup> and Baoyou Geng<sup>ID \*ab</sup>

Reducing carbon dioxide (CO<sub>2</sub>) to high value-added chemicals using renewable electricity is a promising approach to reducing CO<sub>2</sub> levels in the air and mitigating the greenhouse effect, which depends on high-efficiency electrocatalysts. Copper-based catalysts can be used for electroreduction of CO<sub>2</sub> to produce C<sub>2+</sub> products with high added value, but suffer from poor stability and low selectivity. Herein, we propose a strategy to enhance the field effect by varying the cubic corner density on the surface of Cu<sub>2</sub>O microspheres for improving the electrocatalytic performance of CO<sub>2</sub> reduction to C<sub>2+</sub> products. Finite element method (FEM) simulation results show that the high density of cubic corners helps to enhance the local electric field, which increases the K<sup>+</sup> concentration on the catalyst surface. The results of CO<sub>2</sub> electroreduction tests show that the FE<sub>C<sub>2+</sub></sub> of the Cu<sub>2</sub>O catalyst with high-density cubic corners is 71% at a partial current density of 497 mA cm<sup>-2</sup>. Density functional theory (DFT) calculations reveal that Cu<sub>2</sub>O (111) and Cu<sub>2</sub>O (110) can effectively reduce the energy barrier of C-C coupling and improve the FE<sub>C<sub>2+</sub></sub> at high K<sup>+</sup> concentrations relative to Cu<sub>2</sub>O (100). This study provides a new perspective for the design and development of efficient CO<sub>2</sub>RR catalysts.

Received 2nd April 2024  
Accepted 10th June 2024

DOI: 10.1039/d4sc02170c  
[rsc.li/chemical-science](http://rsc.li/chemical-science)

## Introduction

The massive extraction and utilization of fossil fuels has brought about a dramatic increase in the amount of CO<sub>2</sub> in the atmosphere, leading to global warming and climate change, which poses serious environmental problems.<sup>1</sup> The efficient capture and recycling of CO<sub>2</sub> is widely recognized as the key to mitigating environmental problems related to the greenhouse effect and sea level rise, and promoting sustainable development.<sup>2-4</sup> In recent years, it has been found that the electrochemical conversion of CO<sub>2</sub> into C<sub>2+</sub> products with high application value, using renewable electricity, is one of the most promising technologies for realizing the carbon cycle.<sup>5-12</sup> Currently, Cu-based catalysts are attracting attention as the only catalysts that can realize C-C coupling and electroreduction of CO<sub>2</sub> to C<sub>2+</sub> products.<sup>13-21</sup>

Nevertheless, the thermodynamics and kinetics of C-C coupling are relatively slow in the CO<sub>2</sub>RR.<sup>8,22-26</sup> Therefore, modification of Cu-based catalysts, such as crystal surface modulation,<sup>27-29</sup> surface restructuring,<sup>30-33</sup> and oxidation state optimization,<sup>16,34-36</sup> to improve the efficiency of C<sub>2+</sub> products remains a hot topic and challenge. The adjustment of the crystal surface or surface structure has a significant effect on improving the performance of Cu-based catalysts.<sup>37</sup> On the one hand, the exposed faces of Cu-based catalysts have a great influence on the catalytic activity and selectivity in the CO<sub>2</sub>RR process.<sup>38,39</sup> On the other hand, the field effect induced by the tip structure of Cu-based catalysts plays an important role in the CO<sub>2</sub>RR process.<sup>40-42</sup> Numerous studies have found that the active sites of the CO<sub>2</sub>RR are usually located on the top corners and ridges of the catalysts.<sup>43-45</sup> Previous reports have focused on the effects of vertex curvature or array orientation on the field effect; however, the vertices and ridges on the exposed surface are particularly critical to catalytic activity and selectivity, while the effects of vertex density or tip-exposed crystal faces on the catalyst surface for the catalytic performance have been rarely reported, and also their effects on the CO<sub>2</sub>RR are unknown.

Herein, we investigated the effect of the density of cubic corners on the field effect with FEM simulations, and the effect of the vertices and ridges on the cubic corners on the catalytic performance was studied by DFT calculations. The FEM simulation results found that the higher density of the cube corners had a stronger influence on the field effect, which is favorable

<sup>a</sup>College of Chemistry and Materials Science, The Key Laboratory of Functional Molecular Solids, Ministry of Education, The Key Laboratory of Electrochemical Clean Energy of Anhui Higher Education Institutes, Anhui Provincial Engineering Laboratory for New-Energy Vehicle Battery Energy-Storage Materials, Anhui Normal University, Jiuhe Road 189, Wuhu, 241002, China. E-mail: bygeng@mail.ahnu.edu.cn

<sup>b</sup>Institute of Energy, Hefei Comprehensive National Science Center, Hefei, 230031, China

† Electronic supplementary information (ESI) available. See DOI: <https://doi.org/10.1039/d4sc02170c>



for the aggregation and adsorption of  $K^+$ . In the experiment, we prepare a  $Cu_2O$  microsphere with cubic corners on the surface,<sup>46</sup> which is the same as the results of FEM simulation. DFT calculations demonstrate that, at stronger electric fields and higher  $K^+$  concentrations, the  $Cu_2O$  (111) and (110) faces on the cube corner contribute to the adsorption and C–C coupling of \*CO intermediates, as well as to the desorption of  $C_2+$  products. This work fills the gap in the application of the localized electric field induced by different density nano-arrays in  $CO_2$  electroreduction, and also illustrates the roles of vertices and ridges on the exposed crystal in  $CO_2$  electroreduction, which provides new perspectives for the design of efficient  $CO_2$ RR catalysts and contributes to the mitigation of environmental problems caused by greenhouse gases.

## Results and discussion

### FEM simulation

We used COMSOL Multiphysics field simulations to investigate the effect of the density of cubic corners on the local electric field and  $K^+$  concentration. Five models with different cube corner densities (Fig. S1†) were developed using FEM, and the localized electric field and  $K^+$  concentration on their cube corners were also investigated.

As shown in Fig. 1a–c and S2–S4,<sup>†</sup> significant local electric field aggregation effects can be observed for a single cube corner. According to the principle of electric field superposition, as the number of cube corners increases, the electric field strength of the cube angle shows an increasing trend. M3 is a microsphere composed of cubic inflections (Fig. 1c), which has the highest density of cubic corners and the maximum localized electric field strength of  $565\text{ V m}^{-1}$ . We simulated the  $K^+$  concentration on the cubic corner surface using the transport of diluted species (tds) physics modules in COMSOL Multiphysics. From Fig. 1a and

b and S5–S7,<sup>†</sup> it is found that the distribution of  $K^+$  concentration is positively correlated with the distribution of local electric field strength. As the local electric field intensity increases, the  $K^+$  concentration on the cube corner surface gradually increases, with M3 having the maximum  $K^+$  concentration of 3.39 M. The localized electric field facilitates the adsorption and aggregation of  $K^+$ , which is mainly caused by the field effect induced reagent concentration, because positively charged  $K^+$  will be aggregated on the corner surfaces of the cube possessing a strong negative electric field under electrostatic action. The high concentrations of  $K^+$  facilitate the adsorption of  $CO_2$  and the generation of  $C_2+$  products (Fig. 1d).

### Catalyst synthesis and characterization

$Cu_2O$ -X microspheres with cube corners were synthesized using a solvothermal method (X is the volume of water used, which is 0, 0.5, 1, 2, 4, and 10 mL respectively, and the corresponding samples are named  $Cu_2O$ -0,  $Cu_2O$ -0.5,  $Cu_2O$ -1,  $Cu_2O$ -2,  $Cu_2O$ -4, and  $Cu_2O$ -10, respectively). The synthesis mechanism and synthesis process of  $Cu_2O$ -0 are shown in Fig. 2a and S8.<sup>†</sup> In order to better observe the growth mechanism of the  $Cu_2O$ -0 catalyst, its liquid color and product morphology were investigated over time during the synthesis process (Fig. S9†). The scanning electron microscopy (SEM) images of  $Cu_2O$ -0 are shown in Fig. 2b and c, and it can be seen that the surface of  $Cu_2O$ -0 microspheres has a large number of cube corners. The transmission electron microscopy (TEM) image (Fig. 2d) shows more visually that  $Cu_2O$ -0 consists of microspheres with numerous vertices and ridges on the surface. The angles of the vertices are mostly  $90^\circ$ , which better indicates that the tips of the surface on the  $Cu_2O$ -0 microspheres are cubic inflection corners. From the inset in Fig. 2b, the air/water contact angle of  $Cu_2O$ -0 is  $141^\circ$ , which indicates that it has good hydrophobicity. Fig. S10† shows the air/water contact angle of  $Cu_2O$ -X. Fig. 2e–g show the high-resolution TEM (HRTEM) images of  $Cu_2O$ -0. Fig. 2e shows the  $Cu_2O$  crystal planes at the corners of different cubes (as shown in the inset). HRTEM images (Fig. 2f and g) and FFT patterns (inset) show that the lattice spaces are 0.301, 0.246 and 0.213 nm respectively, which can be well matched with the (110), (111) and (200) crystal planes of cubic  $Cu_2O$ . The SEM and HRTEM analyses showed that the morphology of  $Cu_2O$ -X did not change significantly with increasing water content (Fig. S11†). The peaks located at  $29.6^\circ$ ,  $36.4^\circ$ , and  $42.3^\circ$  correspond to the (110), (111), and (200) crystal planes of  $Cu_2O$  (JCPDS: PDF#99-0041), respectively, which indicates that the synthesized material is predominantly  $Cu_2O$  and has a good crystallinity (Fig. 2h). Fig. S12† shows that the  $Cu_2O$ -X catalysts with different water contents have the same  $Cu_2O$  phase. Fig. 2i shows that Cu is predominantly +1-valent, some of which is +2-valent; the  $Cu^{2+}$  in the XPS is most likely caused by the oxidation of the  $Cu_2O$  when it is exposed in the air. In summary, the synthesized catalysts are consistent with the FEM model.

### Electrochemical $CO_2$ RR performance evaluation

Tests of the  $CO_2$  electroreduction properties of the catalysts were performed in a flow cell (Fig. S13†). The linear sweep

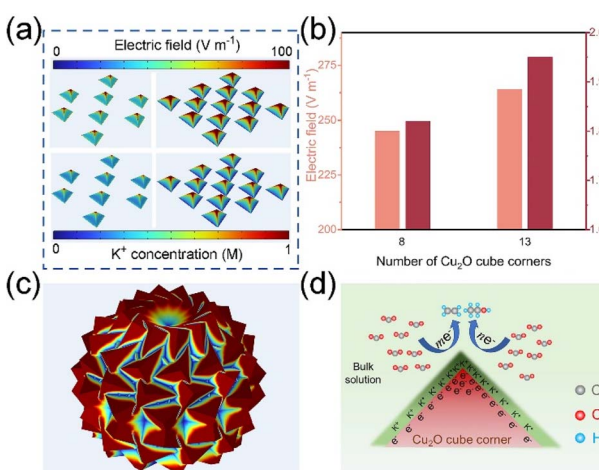


Fig. 1 (a) The electric field (upper half) and  $K^+$  concentration (lower half) distribution on M-4 and M-5 through COMSOL Multiphysics simulations. (b) The electric field and  $K^+$  concentration at the tips of M-4 and M-5. (c) The electric field distribution on M-3. (d) A schematic illustration of the local electric field and  $K^+$  ions on the  $Cu_2O$  cube corner for promoting  $C_2$  formation.



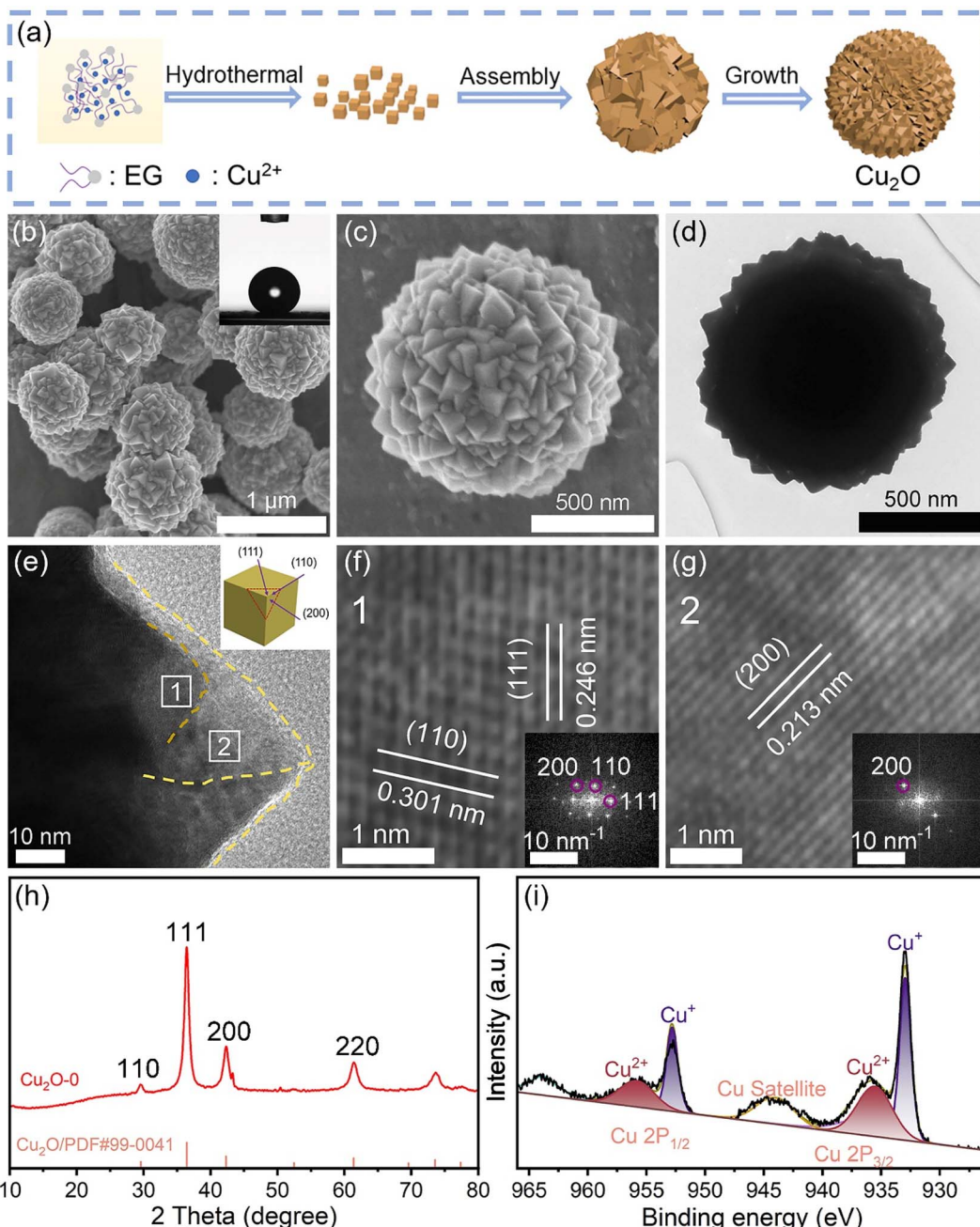


Fig. 2 (a) Schematic formation mechanism of the Cu<sub>2</sub>O-0 catalyst. (b and c) SEM images of the Cu<sub>2</sub>O-0 catalyst. (d) TEM image of the Cu<sub>2</sub>O-0 catalyst. (e–g) HRTEM images of the Cu<sub>2</sub>O-0 catalyst. (h) The XRD pattern of the Cu<sub>2</sub>O-0 catalyst. (i) The XPS spectrum of the Cu<sub>2</sub>O-0 catalyst.

voltammetry (LSV) test results (Fig. 3a and S14†) show that Cu<sub>2</sub>O-0 has greater positive onset potential and greater negative current density, indicating that Cu<sub>2</sub>O-0 has higher CO<sub>2</sub>RR activity. The liquid and gas products were examined by <sup>1</sup>H NMR spectroscopy (Fig. S15†) and gas chromatography (GC) (Fig. S16 and S17†), respectively. In terms of product distribution, the reduction products of all Cu<sub>2</sub>O-X catalysts had the same trend with increasing applied current, with the faradaic efficiency (FE) of C<sub>2+</sub> increasing and then decreasing, and the FE of H<sub>2</sub> decreasing and then increasing (Fig. 3b and S18†). From Fig. 3c and d, it was found that the Cu<sub>2</sub>O-0 catalyst possessed the

largest FE<sub>C<sub>2+</sub></sub> and the smallest FE<sub>H<sub>2</sub></sub>. The FE<sub>C<sub>2+</sub></sub> and FE<sub>H<sub>2</sub></sub> of the Cu<sub>2</sub>O-0 catalyst were 71% and 12% at a partial current density of 497 mA cm<sup>-2</sup>, respectively. Moreover, the FE<sub>C<sub>2+</sub></sub> of the Cu<sub>2</sub>O-0 catalyst was 1.8 times higher than the FE<sub>C<sub>2+</sub></sub> of the Cu<sub>2</sub>O-10 catalyst.

We have conducted multiple studies to better understand the differences in catalytic performance of different Cu<sub>2</sub>O-X catalysts. By recording the cyclic voltammetry curves (Fig. S19†) of Cu<sub>2</sub>O-X catalysts at different scan rates in the non-Faraday zone, their double-layer capacitance ( $C_{dl}$ ) (Fig. S20†) was calculated, which was used to estimate their surface roughness



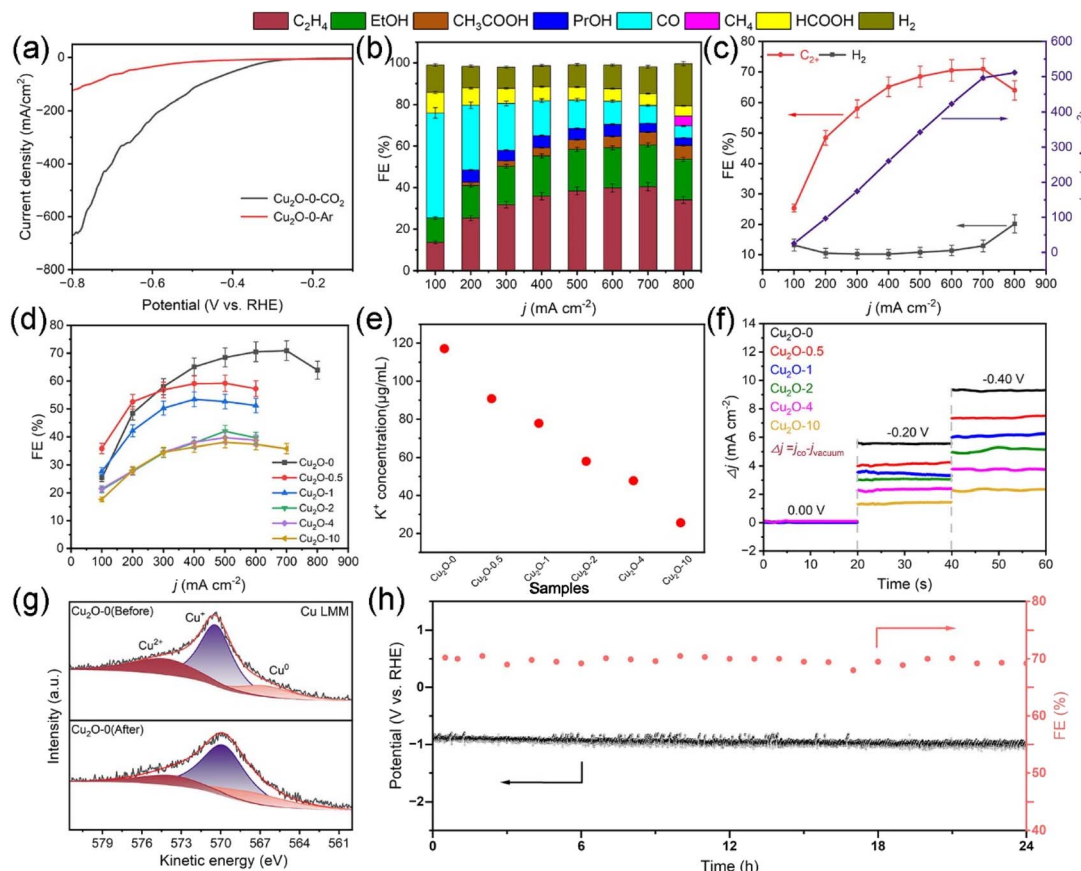


**Fig. 3** (a) The LSV curves of the Cu<sub>2</sub>O-0 catalyst under an N<sub>2</sub> atmosphere and CO<sub>2</sub> atmosphere. (b) FEs of various products on the Cu<sub>2</sub>O-0 catalyst during the CO<sub>2</sub>RR at different current densities. (c) C<sub>2+</sub> and H<sub>2</sub> FEs and current densities vs. applied potential of the Cu<sub>2</sub>O-0 catalyst. (d) C<sub>2+</sub> FEs of Cu<sub>2</sub>O-X catalysts. (e) Comparison of the adsorbed-K<sup>+</sup> concentration on Cu<sub>2</sub>O-X catalysts. (f) Results of CO adsorption responses on Cu<sub>2</sub>O-X catalysts under different applied voltages. (g) Deconvoluted Cu Auger LMM spectra of the Cu<sub>2</sub>O-0 catalyst before and after the CO<sub>2</sub>RR. (h) CO<sub>2</sub>RR stability on the Cu<sub>2</sub>O-0 catalyst at 700 mA cm<sup>-2</sup>.

coefficient ( $R_f$ ) and electrochemically active surface area (ECSA) (Fig. S21 and Table S1†). The results showed that the Cu<sub>2</sub>O-0 catalyst had the largest  $C_{dl}$  (42.8 mF cm<sup>-2</sup>),  $R_f$  (713.3), and ECSA (713.3 cm<sup>2</sup>), thus indicating that the Cu<sub>2</sub>O-0 catalyst can produce more active sites than other Cu<sub>2</sub>O-X catalysts, which is more favorable for the CO<sub>2</sub>RR. Meanwhile, Fig. S22† shows that the Cu<sub>2</sub>O-0 catalyst has the smallest Tafel slope, which also indicates that the Cu<sub>2</sub>O-0 catalyst has the best CO<sub>2</sub>RR performance.

According to the FEM simulation results, it is illustrated that the high density of cubic corners contributes to the adsorption of K<sup>+</sup> and CO. To validate the FEM simulation results and to demonstrate the advantages of high-density cubic corners, we performed K<sup>+</sup> and CO adsorption experiments (schematic shown in Fig. S23 and S24†). Fig. 3e and f and Table S2† show that the adsorption capacity of K<sup>+</sup> and CO on the Cu<sub>2</sub>O-X catalysts increases gradually with the increase of the cube corner density, and the Cu<sub>2</sub>O-0 catalyst has the largest cube corner density and the strongest K<sup>+</sup> and CO adsorption capacity.

As shown in Fig. 3h, the Cu<sub>2</sub>O-0 catalyst also exhibited excellent long-term stability, operating at a constant current density of 700 mA cm<sup>-2</sup> for 24 h without a significant change in

the applied voltage or FE<sub>C<sub>2+</sub></sub>, with the FE<sub>C<sub>2+</sub></sub> remaining around 70%. In order to better understand the long-term stability and selectivity of the Cu<sub>2</sub>O-0 catalyst, SEM, XRD, and XPS were used to characterize the Cu<sub>2</sub>O-X catalyst before and after the CO<sub>2</sub>RR. From Fig. S25,† the morphology of the Cu<sub>2</sub>O-0 catalyst was almost unchanged before and after the CO<sub>2</sub>RR. XRD (Fig. S26 and S27†) patterns showed that the physical phase of the Cu<sub>2</sub>O-0 catalyst was maintained before and after the reaction. The Cu Auger LMM spectra (Fig. 3g and S28†) were recorded and deconvoluted to distinguish Cu<sup>+</sup> and Cu<sup>0</sup> before and after the CO<sub>2</sub>RR.<sup>47</sup> The ratio of the Cu<sup>0</sup> fraction increased from 17.14% to 20.23%, and the ratio of the Cu<sup>+</sup> fraction decreased from 68.72% to 65.34% in the Cu<sub>2</sub>O-0 catalyst. The Cu Auger LMM spectra illustrated that Cu<sup>+</sup> in the Cu<sub>2</sub>O-0 catalyst was well maintained during the CO<sub>2</sub>RR process. The reason for Cu<sup>+</sup> being maintained in the Cu<sub>2</sub>O-0 catalyst may be due to the high density of cubic corners on the Cu<sub>2</sub>O-0 catalyst microspheres, which gives the surface a strong localized electric field and high K<sup>+</sup> concentration, leading to accelerated electron transport on the cubic corner surface and the inhibition of the redox reaction of Cu<sup>+</sup>/Cu<sup>0</sup>.<sup>47</sup> These lead to the excellent selectivity and long-term stability of the Cu<sub>2</sub>O-0 catalyst.

***In situ* Raman and *in situ* FT-IR measurements**

To further understand the reaction mechanism of the CO<sub>2</sub>RR, we performed *in situ* Raman and *in situ* FT-IR tests on the Cu<sub>2</sub>O-0 and Cu<sub>2</sub>O-4 during the CO<sub>2</sub>RR. The *in situ* Raman testing equipment is shown in Fig. S29.† As shown in Fig. 4a and S30a,† Cu<sub>2</sub>O-0 and Cu<sub>2</sub>O-4 show two peaks around  $\sim 280$  and  $\sim 365$  cm<sup>-1</sup>, which are caused by the rotational and stretching vibrations of \*CO on the Cu active site after applying the voltage.<sup>48–50</sup> In addition, the Cu<sub>2</sub>O-0 and Cu<sub>2</sub>O-4 catalysts have three peaks associated with Cu<sup>δ+</sup> near  $\sim 415$ ,  $\sim 520$ , and  $\sim 620$  cm<sup>-1</sup> in the low-energy region (Fig. 4b and S30b†), corresponding to the modes resulting from a multi-phonon process – the T<sub>2g</sub> vibrational mode and the T<sub>1u</sub> mode of Cu<sub>2</sub>O.<sup>47,49,51–55</sup> With the increase of applied potential, the Cu<sup>+</sup> characteristic peaks ( $\sim 520$  cm<sup>-1</sup>) of Cu<sub>2</sub>O-0 catalysts are well preserved, and this is consistent with the XRD (Fig. S26†) and XPS (Fig. 3g) results measured before and after the CO<sub>2</sub>RR, fully indicating that the Cu valence state in the Cu<sub>2</sub>O-0 catalyst is stable during the CO<sub>2</sub>RR process. In the high-energy region, the signals near  $\sim 1015$  and  $\sim 1066$  cm<sup>-1</sup> are attributed to the adsorption of HCO<sub>3</sub><sup>-</sup> and CO<sub>3</sub><sup>2-</sup> (Fig. 4c and S30c†),<sup>50,56</sup> respectively, which are formed on the surface of the catalyst after CO<sub>2</sub> is dissolved in the electrolyte. The local hydrogen proton concentration and local microenvironment around the catalysts during the CO<sub>2</sub>RR were evaluated by monitoring the ratio of HCO<sub>3</sub><sup>-</sup> and CO<sub>3</sub><sup>2-</sup> adsorbed on the catalyst surface (Fig. S31†).<sup>56,57</sup> The results show that the local hydrogen proton

depletion on the surface of the Cu<sub>2</sub>O-0 catalyst is more stable than that of the Cu<sub>2</sub>O-4 catalyst, thus maintaining the stability of the local microenvironment and the durability of the C<sub>2+</sub> products on the catalyst.<sup>50</sup> In addition, the signals generated in the regions around  $\sim 1840$  cm<sup>-1</sup> and  $\sim 2060$  cm<sup>-1</sup> belong to the bridge-boundary \*CO (\*CO<sub>bridge</sub>) and top-boundary \*CO (\*CO<sub>atop</sub>) conformations,<sup>48,58</sup> respectively. As the cathode applied voltage became more negative, the \*CO<sub>bridge</sub> signal on the Cu<sub>2</sub>O-0 catalyst changed weakly (Fig. 4d), and the \*CO<sub>bridge</sub> signal on the Cu<sub>2</sub>O-4 catalyst basically disappeared (Fig. S30d†), suggesting that most of the \*CO intermediates were bound at the top and a small portion of them were bound at the bridge sites in the Cu<sub>2</sub>O-0 catalyst, whereas the \*CO intermediates were mainly from the top of the Cu<sub>2</sub>O-4 catalyst. The mixing of \*CO<sub>bridge</sub> and \*CO<sub>atop</sub> is more favorable for the C–C coupling.<sup>59,60</sup> Therefore, the \*CO intermediates on the Cu<sub>2</sub>O-0 catalyst are more favorable for C–C coupling and the production of C<sub>2+</sub> products.

The \*CO<sub>atop</sub> intermediates on the catalyst can be divided into low and high frequency bands (LFB and HFB). According to previous studies, the signal in the LFB belongs to a dynamic \*CO intermediate, which contributes to subsequent C–C coupling. The HFB stretching band is attributed to the separated static \*CO intermediate, which makes it difficult to perform C–C coupling.<sup>48,60</sup> As seen in Fig. 4e, we compared the LFB and HFB band intensities. The low/high value of the Cu<sub>2</sub>O-0 catalyst is larger than that of the Cu<sub>2</sub>O-4 catalyst, indicating

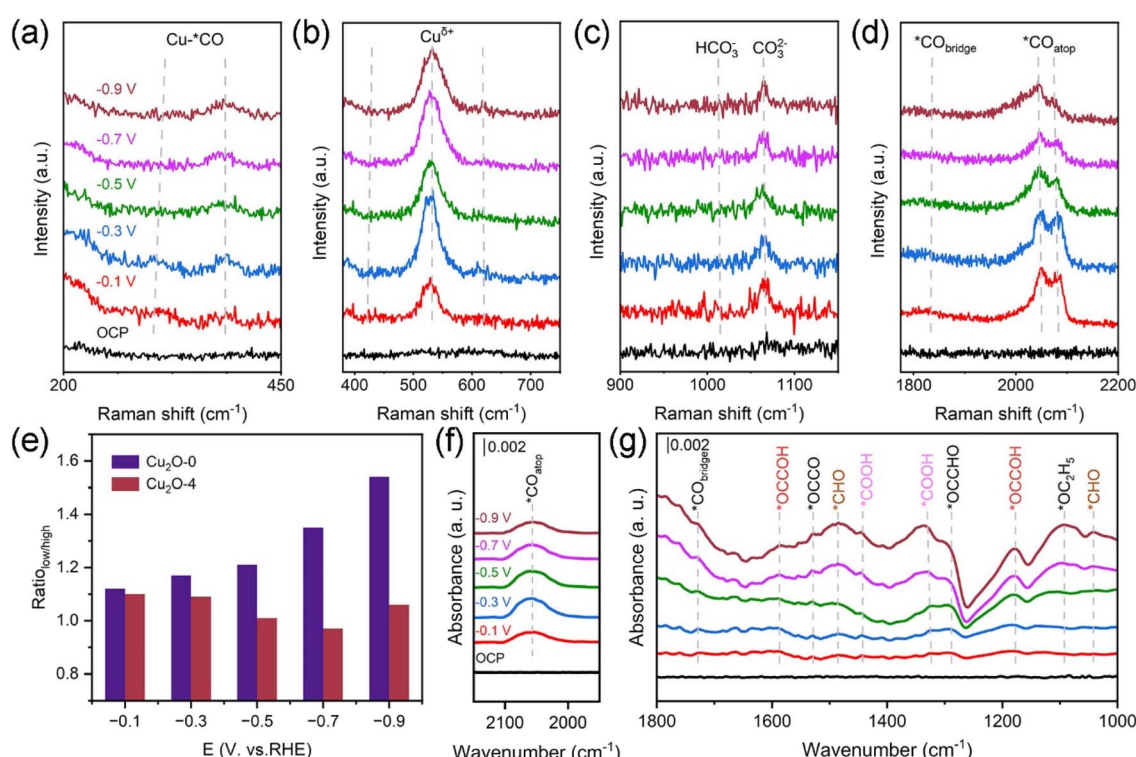


Fig. 4 *In situ* Raman spectra of the Cu<sub>2</sub>O-0 catalyst in the range 200–450 cm<sup>-1</sup> (a), 400–750 cm<sup>-1</sup> (b), 900–1150 cm<sup>-1</sup> (c) and 1800–2200 cm<sup>-1</sup> (d) at various applied potentials (vs. RHE). (e) Ratio of the low-frequency and high-frequency bands in the range 2000–2200 cm<sup>-1</sup> of Cu<sub>2</sub>O-0 and Cu<sub>2</sub>O-4 catalysts at various applied potentials. (f and g) *In situ* FT-IR spectra of the Cu<sub>2</sub>O-0 catalyst at various applied potentials (vs. RHE).



that the  $\text{Cu}_2\text{O}$ -0 catalyst is more favorable for C-C coupling and  $\text{C}_{2+}$  product generation.<sup>50</sup> Through observing the changes in the intensity of the  ${}^*\text{CO}_{\text{atop}}$  peaks, it is found that as the external applied voltage becomes more negative, the  ${}^*\text{CO}$  intermediates first accumulate, then C-C coupling generates  $\text{C}_{2+}$  products on the  $\text{Cu}_2\text{O}$ -0 catalyst. Due to the involvement of more  ${}^*\text{CO}$  intermediates in C-C coupling, the  ${}^*\text{CO}$  peak intensity shows a decreasing trend on the  $\text{Cu}_2\text{O}$ -0 catalyst (Fig. 4d),<sup>61</sup> while the relative intensity of the HFB (Fig. S30d†) tends to increase at higher potentials on the  $\text{Cu}_2\text{O}$ -4 catalyst, indicating an increase in static  ${}^*\text{CO}$  intermediates and a decrease in C-C coupling ability on the  $\text{Cu}_2\text{O}$ -4 catalyst.<sup>48</sup> This is consistent with the electrochemical  $\text{CO}_2$ RR results.

*In situ* FT-IR tests was performed to investigate the reaction pathways of the  $\text{C}_{2+}$  products (Fig. S32†). In Fig. 4f and g and S33,† the peaks at  $\sim 1720$  and  $\sim 2050 \text{ cm}^{-1}$  are the characteristic peaks of  ${}^*\text{CO}_{\text{bridge}}$  and  ${}^*\text{CO}_{\text{atop}}$ ,<sup>62,63</sup> respectively. This is the same species of  ${}^*\text{CO}$  intermediates observed in *in situ* Raman spectra. The characteristic peaks at  $\sim 1330$  and  $\sim 1440 \text{ cm}^{-1}$  belong to the C-OH and C-O stretching modes of  ${}^*\text{COOH}$  intermediates, respectively, which help to generate  ${}^*\text{CO}$  intermediates on the catalysts.<sup>64,65</sup> Compared with  $\text{Cu}_2\text{O}$ -4, the  ${}^*\text{COOH}$  peak intensity on  $\text{Cu}_2\text{O}$ -0 is significantly stronger, but its  ${}^*\text{CO}_{\text{atop}}$  peak intensity is weak, indicating that the  ${}^*\text{CO}$  intermediates produced by  ${}^*\text{COOH}$  on  $\text{Cu}_2\text{O}$ -0 are more involved in C-C coupling and  $\text{C}_{2+}$  products.<sup>66</sup> The absorption peaks near  $\sim 1090$ ,  $\sim 1180$  and  $\sim 1590 \text{ cm}^{-1}$  are attributed to  ${}^*\text{OC}_2\text{H}_5$  and  ${}^*\text{OCCOH}$  intermediates, respectively, which are key intermediates of  $\text{C}_{2+}$  products.<sup>56,63,67</sup> The  ${}^*\text{OCCO}$  intermediates appear at  $\sim 1530 \text{ cm}^{-1}$ , indicating that the C-C coupling mode on the catalyst is likely due to dimerization of the  ${}^*\text{CO}$  intermediate, leading to further

hydrogenation into  ${}^*\text{OCCOH}$ .<sup>68–70</sup> As the applied voltage becomes more negative, the accumulation of  ${}^*\text{CHO}$  ( $\sim 1041$  and  $\sim 1480 \text{ cm}^{-1}$ ) and the weakening of  ${}^*\text{OCCHO}$  ( $\sim 1290 \text{ cm}^{-1}$ ) peak intensity on the  $\text{Cu}_2\text{O}$ -0 catalyst indicate that it is difficult to achieve C-C coupling of  ${}^*\text{CO} + {}^*\text{CHO}$ , which also indirectly confirms that the C-C coupling mode is  ${}^*\text{CO} + {}^*\text{CO}$ .<sup>62,71</sup>

The performance differences between  $\text{Cu}_2\text{O}$ -0 and  $\text{Cu}_2\text{O}$ -4 were understood by in-depth analysis of  ${}^*\text{CO}$  intermediates. Research findings suggest that the intermixing of  ${}^*\text{CO}_{\text{bridge}}$  and  ${}^*\text{CO}_{\text{atop}}$  was more favorable for the production of the  $\text{C}_{2+}$  products, which may be due to the ease of  ${}^*\text{CO}_{\text{bridge}}$  in promoting  ${}^*\text{CO}$  dimerization.<sup>72</sup> With the increase of negative voltage, the intensity of  ${}^*\text{CO}_{\text{bridge}}$  on  $\text{Cu}_2\text{O}$ -0 does not change obviously, but the intensity of the  ${}^*\text{CO}_{\text{atop}}$  first enhances and then decreases, indicating that  ${}^*\text{CO}$  intermediates accumulate first, and then more  ${}^*\text{CO}$  intermediates participate in the C-C coupling process on  $\text{Cu}_2\text{O}$ -0.<sup>63</sup> The change trend of  ${}^*\text{CO}_{\text{atop}}$  on the  $\text{Cu}_2\text{O}$ -0 catalyst in the *in situ* FT-IR spectrum is consistent with its *in situ* Raman spectrum (Fig. 4d). However, as the applied voltage increases, the  ${}^*\text{CO}_{\text{bridge}}$  peak ( $\sim 1720 \text{ cm}^{-1}$ ) of the  $\text{Cu}_2\text{O}$ -4 catalyst decreases and almost disappears. At the same time, the intensity of the  ${}^*\text{CO}_{\text{atop}}$  peak ( $\sim 2050 \text{ cm}^{-1}$ ) gradually increases (Fig. S33†), indicating that C-C coupling occurs with difficulty on the  $\text{Cu}_2\text{O}$ -4 catalyst.<sup>63</sup> The results of *in situ* FT-IR are consistent with those of *in situ* Raman and electrochemical  $\text{CO}_2$ RR.

### DFT theoretical calculations

DFT theoretical calculations were used to gain a deeper understanding of the mechanism of  $\text{Cu}_2\text{O}$ -X catalysts promoting the electro-reduction of  $\text{CO}_2$  to  $\text{C}_{2+}$  products. We

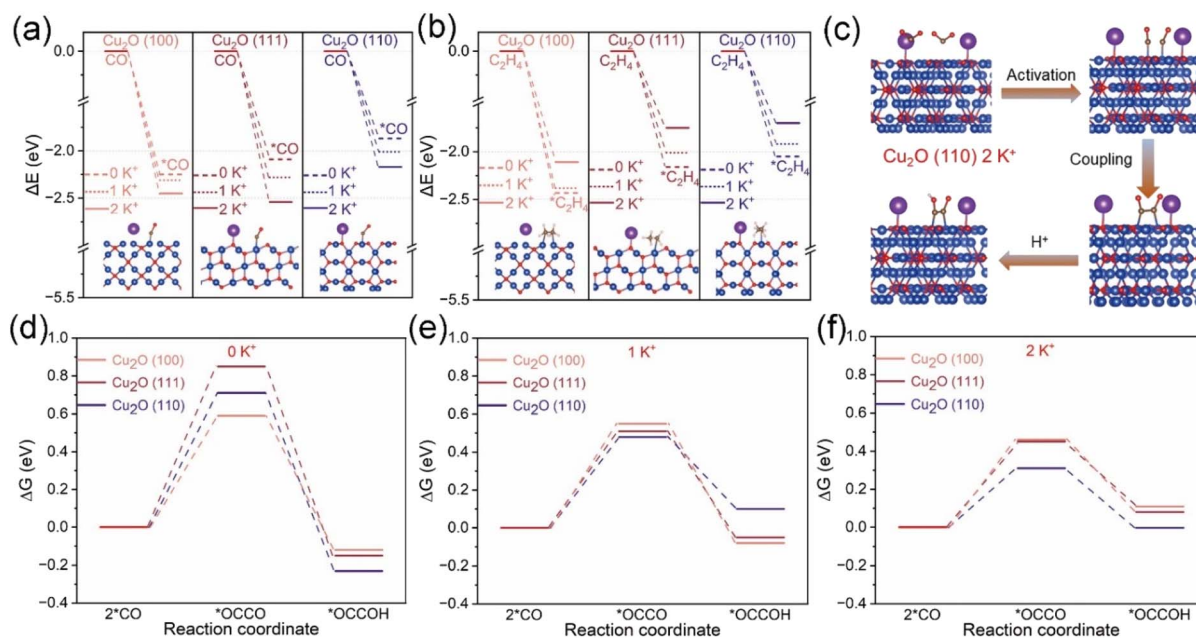


**Fig. 5** Adsorption energies of (a)  $\text{CO}$  and (b)  $\text{C}_2\text{H}_4$  on three crystalline surfaces of  $\text{Cu}_2\text{O}$  (100), (111) and (110) at three  $\text{K}^+$  concentrations of 0  $\text{K}^+$ , 1  $\text{K}^+$  and 2  $\text{K}^+$ , respectively. (c) Adsorption configurations of reaction intermediates on the  $\text{Cu}_2\text{O}$  (110) structure at the  $\text{K}^+$  concentrations of 2  $\text{K}^+$ . Gibbs free energy pathways for C-C coupling on three crystalline surfaces of  $\text{Cu}_2\text{O}$  (100), (111) and (110) at three  $\text{K}^+$  concentrations of 0  $\text{K}^+$  (d), 1  $\text{K}^+$  (e) and 2  $\text{K}^+$  (f), respectively.



performed DFT calculations to investigate the adsorption capacity of the reaction intermediate  $^*\text{CO}$  and the product  $\text{C}_2\text{H}_4$  at the  $\text{Cu}_2\text{O}$  (100), (111) and (110) interface at different  $\text{K}^+$  concentrations as well as the Gibbs free energy of the C–C coupling. We developed a DFT model of the same  $\text{Cu}_2\text{O}$  crystal surface as the catalyst under study (Fig. S34 $\dagger$ ). As shown in Fig. 5a and b and S35–S40, and Tables S3 and S4, $\dagger$   $^*\text{CO}$  and  $^*\text{C}_2\text{H}_4$  adsorption on the  $\text{Cu}_2\text{O}$  (100) crystallite were stronger than that on  $\text{Cu}_2\text{O}$  (111) and (110) crystallites. It was very difficult for  $\text{C}_2\text{H}_4$  to overflow from the  $\text{Cu}_2\text{O}$  (100) crystal surface, so the amount of  $\text{C}_{2+}$  product produced by the  $\text{Cu}_2\text{O}$  (100) crystal surface was low. Unlike the  $\text{Cu}_2\text{O}$  (100) crystal faces, the adsorption of  $^*\text{CO}$  was weaker on the  $\text{Cu}_2\text{O}$  (111) and (110) crystal faces, but the introduction of  $\text{K}^+$  led to the enhancement of  $^*\text{CO}$  adsorption; at the same time, the adsorption of  $^*\text{C}_2\text{H}_4$  on the  $\text{Cu}_2\text{O}$  (111) and (110) crystal faces was weaker, and the  $\text{C}_2\text{H}_4$  produced was readily desorbed out from the  $\text{Cu}_2\text{O}$  (111) and (110) crystal faces, so the amount of  $\text{C}_{2+}$  product produced by the  $\text{Cu}_2\text{O}$  (111) and (110) crystal faces was higher.

From the *in situ* characterization and DFT calculations (Fig. S41 $\dagger$ ), the pathway diagram of the  $\text{Cu}_2\text{O}-\text{X}$  catalyst to generate  $\text{C}_{2+}$  products was constructed and is shown in Fig. S42. $\dagger$ <sup>61</sup> The critical step to generate  $\text{C}_{2+}$  products is the coupling of two  $^*\text{CO}$  intermediates into  $^*\text{OCCO}$  intermediates. Fig. 5c shows the schematic diagram of the  $\text{CO}_2\text{RR}$  on the  $\text{Cu}_2\text{O}$  (110) crystal surface under 2  $\text{K}^+$  concentration. Fig. S43–S45 $\dagger$  are schematic diagrams of the modeling of C–C coupling as well as hydrogenation. From Fig. 5d–f and S46–S49, and Table S5, $\dagger$  it is found that the Gibbs free energies of C–C coupling on all three crystalline surfaces of  $\text{Cu}_2\text{O}$  (100), (111) and (110) are decreasing with the increase of  $\text{K}^+$  concentration. The Gibbs free energy of C–C coupling on the  $\text{Cu}_2\text{O}$  (110) (0.31 eV) and (111) (0.45 eV) crystal surfaces is smaller than that on the  $\text{Cu}_2\text{O}$  (100) (0.46 eV) crystal surface at 2  $\text{K}^+$  concentration, which suggests that the  $\text{Cu}_2\text{O}$  (110) and (111) crystal surfaces are more favorable for C–C coupling at high  $\text{K}^+$  concentration. At the same time, experimental support was provided for the DFT calculation results (Fig. S50 $\dagger$ ). In the experiment,  $\text{Cu}_2\text{O}$  catalysts with different crystal planes were synthesized and the electrocatalytic  $\text{CO}_2$  reduction performance was studied. It was found that the experimental results were consistent with the DFT calculation results.

## Conclusions

In summary, we propose a strategy to enhance the field effect and thus improve the catalyst's performance for the electro-reduction of  $\text{CO}_2$  by changing the density of cubic corner arrays on the catalyst surface.  $\text{CO}_2\text{RR}$  experimental results indicated that the  $\text{FE}_{\text{C}_{2+}}$  of the  $\text{Cu}_2\text{O}$  catalyst with high-density cubic corners was 71% at a partial current density of  $497 \text{ mA cm}^{-2}$ , and the  $\text{FE}_{\text{C}_{2+}}$  of this  $\text{Cu}_2\text{O}-\text{O}$  catalyst was 1.8 times higher than the  $\text{FE}_{\text{C}_{2+}}$  of the microcubic  $\text{Cu}_2\text{O}$  catalyst. Moreover, the cubic corner arrays on the surface of  $\text{Cu}_2\text{O}$  microspheres help to improve the hydrophobicity of the catalyst and reduce the occurrence of its competing HER. FEM simulations and DFT calculations demonstrated that the high density of cubic

corners contributed to the enhancement of the local electric field, which increased the  $\text{K}^+$  concentration in the local micro-environment and enhanced the adsorption of  $^*\text{CO}$  intermediates on the catalyst surface. The increase in the density of cubic corners leads to a higher number of vertices ( $\text{Cu}_2\text{O}$  (111)) and ridges ( $\text{Cu}_2\text{O}$  (110)). Relative to  $\text{Cu}_2\text{O}$  (100),  $\text{Cu}_2\text{O}$  (111) and  $\text{Cu}_2\text{O}$  (110) can effectively reduce the energy barrier of C–C coupling and improve the Faraday efficiency of  $\text{C}_{2+}$  products at high  $\text{K}^+$  concentrations. This strategy can not only effectively improve the  $\text{CO}_2\text{RR}$  performance of the catalysts, but also indicates that the surface structure of the catalysts plays an important role in their  $\text{CO}_2\text{RR}$  performance, which provides a new idea for the design of efficient  $\text{CO}_2\text{RR}$  catalysts.

## Data availability

Data supporting the findings of this study are available within the article ESI. $\dagger$

## Author contributions

Hu Zang: conceptualization, data curation, formal analysis, investigation, methodology, software, writing – original draft, and writing – review & editing; Changjiang Liu, Qinyuan Ji, Jiahao Wang, and Haiyan Lu: data curation, formal analysis, investigation, and software; Nan Yu: investigation, methodology, software and validation; Baoyou Geng: conceptualization, formal analysis, investigation, methodology, resources, funding acquisition, supervision, project administration, and writing – review & editing.

## Conflicts of interest

The authors declare no conflicts of interest.

## Acknowledgements

We thank the National Natural Science Foundation of China (22171005), the Anhui Province Outstanding Research and Innovation Team Project for Universities (2023AH010030), and the University Synergy Innovation Program of Anhui Province (GXXT-2020-005, GXXT-2021-012, GXXT-2021-013, and GXXT-2022-007) for supporting this work.

## References

- 1 P. Falkowski, R. J. Scholes and E. Boyle, *Science*, 2000, **290**, 291–296.
- 2 B. Obama, *Science*, 2017, **355**, 126–129.
- 3 A. J. Welch, E. Dunn and J. S. Duchene, *ACS Energy Lett.*, 2020, **5**, 940–945.
- 4 X. Tan, C. Yu and Y. Ren, *Energy Environ. Sci.*, 2021, **14**, 765–780.
- 5 L. P. De, C. Hahn, D. Higgins, S. A. Jaffer, T. F. Jaramillo and E. H. Sargent, *Science*, 2019, **364**, eaav3506.



6 O. S. Bushuyev, L. P. De, C. T. Dinh, L. Tao, G. Saur, J. Lagemaat, S. O. Kelley and E. H. Sargent, *Joule*, 2018, **2**, 825–832.

7 T. M. Gür, *Energy Environ. Sci.*, 2018, **11**, 2696–2767.

8 D. F. Gao, R. M. Aran-ais and H. S. Jeon, *Nat. Catal.*, 2019, **2**, 198–210.

9 A. D. Handoko, F. X. Wei, Jenndy, S. Y. Boon and W. S. Zhi, *Nat. Catal.*, 2018, **1**, 922–934.

10 X. Mao, T. W. He, G. Kour, H. Q. Yin, C. Y. Ling, G. P. Gao, Y. G. Jin, Q. J. Liu, A. P. O'Mullane and A. J. Du, *Chem. Sci.*, 2024, **15**, 3330–3338.

11 H. R. M. Jhong, S. Ma and P. J. A. Kenis, *Curr. Opin. Chem. Eng.*, 2013, **2**, 191–199.

12 L. Zhu, Y. Lin, K. Liu, E. Cortes, H. Li, J. Hu, A. Yamaguchi, X. Liu, M. Miyauchi, J. Fu and M. Liu, *Chin. J. Catal.*, 2021, **42**, 1500–1508.

13 X. Zhi, Y. Jiao, Y. Zheng, K. Davey and S. Z. Qiao, *J. Mater. Chem. A*, 2021, **9**, 6345–6351.

14 T. Zhang, Z. Li, J. Zhang and J. Wu, *J. Catal.*, 2020, **387**, 163–169.

15 Y. C. Li, E. P. Delmo, G. Y. Hou, X. L. Cui, M. Zhao, Z. H. Tian, Y. Zhang and M. H. Shao, *Angew. Chem., Int. Ed.*, 2023, e202313522.

16 K. Yao, Y. Xia, J. Li, N. Wang, J. Han, C. Gao, M. Han, G. Shen, Y. Liu, A. Seifitokaldani, X. Sun and H. Liang, *J. Mater. Chem. A*, 2020, **8**, 11117–11123.

17 Y. D. Wang, R. Y. Zhao, Y. P. Liu, F. T. Zhang, Y. P. Wang, Z. H. Wu, B. X. Han and Z. M. Liu, *Chem. Sci.*, 2024, **15**, 4140–4145.

18 Z. Gu, H. Shen, Z. Chen, Y. Yang, C. Yang, Y. Ji, Y. Wang, C. Zhu, J. Liu, J. Li, T.-K. Sham, X. Xu and G. Zheng, *Joule*, 2021, **5**, 429–440.

19 H. Li, T. Liu, P. Wei, L. Lin, D. Gao, G. Wang and X. Bao, *Angew. Chem., Int. Ed.*, 2021, **60**, 14329–14333.

20 X. Zhang, K. Liu, J. Fu, H. Li, H. Pan, J. Hu and M. Liu, *Front. Phys.*, 2021, **16**, 63500.

21 B. Yang, K. Liu, H. Li, C. Liu, J. Fu, H. Li, J. E. Huang, P. Ou, T. Alkayyali and C. Cai, *J. Am. Chem. Soc.*, 2022, **144**, 3039–3049.

22 X. Zhang and Z. Zhou, *J. Phys. Chem. C*, 2022, **126**, 3820–3829.

23 S. Nitopi, E. Bertheussen, S. B. Scott, X. Liu, A. K. Engstfeld, S. Horch, B. Seger, I. E. L. Stephens, K. Chan, C. Hahn, J. K. Nørskov, T. F. Jaramillo and I. Chorkendorff, *Chem. Rev.*, 2019, **119**, 7610–7672.

24 G. Wang, J. Chen, Y. Ding, P. Cai, L. Yi, Y. Li, C. Tu, Y. Hou, Z. Wen and L. Dai, *Chem. Soc. Rev.*, 2021, **50**, 4993–5061.

25 M. B. Ross, P. De Luna, Y. Li, C. T. Dinh, D. Kim, P. Yang and E. H. Sargent, *Nat. Catal.*, 2019, **2**, 648–658.

26 X. Hu, S. Yao, L. T. Chen, X. Zhang, M. G. Jiao, Z. Y. Lu and Z. Zhou, *J. Mater. Chem. A*, 2021, **9**, 23515–23521.

27 P. S. Li, J. H. Bi, J. Y. Liu, Q. G. Zhu, C. J. Chen, X. F. Sun, J. L. Zhang, Z. M. Liu and B. X. Han, *Chem. Sci.*, 2023, **14**, 310–316.

28 K. Jiang, Y. Huang, G. Zeng, F. M. Toma, W. A. Goddard and A. T. Bell, *ACS Energy Lett.*, 2020, **5**, 1206–1214.

29 C. Tang, J. Shi, X. Bai, A. Hu, N. Xuan, Y. Yue, T. Ye, B. Liu, P. Li, P. Zhuang, J. Shen, Y. Liu and Z. Sun, *ACS Catal.*, 2020, **10**, 2026–2032.

30 Y. Wang, H. Shen, K. J. T. Livi, D. Raciti, H. Zong, J. Gregg, M. Onadeko, Y. Wan, A. Watson and C. Wang, *Nano Lett.*, 2019, **19**, 8461–8468.

31 Z. Sun, J. Dong, C. Chen, S. Zhang and Y. Zhu, *J. Chem. Technol. Biotechnol.*, 2021, **96**, 1161–1175.

32 Y. Zhou, F. Che, M. Liu, C. Zou, Z. Liang, P. De Luna, H. Yuan, J. Li, Z. Wang and H. Xie, *Nat. Chem.*, 2018, **10**, 974–980.

33 X. Tan, H. J. Zhu, C. He, Z. W. Zhuang, K. A. Sun, C. Zhang and C. Chen, *Chem. Sci.*, 2024, **15**, 4292–4312.

34 Y. Wang, P. Han, X. Lv, L. Zhang and G. Zheng, *Joule*, 2018, **2**, 2551–2582.

35 S. Y. Lee, S. Y. Chae, H. Jung, C. W. Lee, D. L. T. Nguyen, H. S. Oh, B. K. Min and Y. J. Hwang, *J. Mater. Chem. A*, 2020, **8**, 6210–6218.

36 L. P. De, B. R. Quintero, C. T. Dinh, M. B. Ross, O. S. Bushuyev, P. Todorovic, T. Regier, S. O. Kelley, P. Yang and E. H. Sargent, *Nat. Catal.*, 2018, **1**, 103–110.

37 Y. Y. Xue, Y. B. Guo, H. J. Cui and Z. Zhou, *Small Methods*, 2021, **5**, 2100736.

38 H. Zhang, C. H. He, S. M. Han, Z. Y. Du, L. Wang, Q. B. Yun, W. B. Cao, B. W. Zhang, Y.-H. Tian and Q. P. Lu, *Chin. Chem. Lett.*, 2022, **33**, 3641–3649.

39 Y. G. Gao, Q. Wu, X. Z. Liang, Z. Y. Wang, Z. K. Zheng, P. Wang, Y. Y. Liu, Y. Dai, M.-H. Whangbo and B. B. Huang, *Adv. Sci.*, 2020, **7**, 1902820.

40 M. Liu, Y. Pang, B. Zhang, P. De Luna, O. Voznyy, J. Xu, X. Zheng, C. T. Dinh, F. Fan, C. Cao, F. P. de Arquer, T. S. Safaei, A. Mepham, A. Klinkova, E. Kumacheva, T. Fillete, D. Sinton, S. O. Kelley and E. H. Sargent, *Nature*, 2016, **537**, 382–386.

41 Y. J. Zhou, Y. Q. Liang, J. W. Fu, K. Liu, Q. Chen, X. Q. Wang, H. M. Li, L. Zhu, J. H. Hu, H. Pan, M. Miyauchi, L. X. Jiang, E. Cortés and M. Liu, *Nano Lett.*, 2022, **22**, 1963–1970.

42 Z. Z. Niu, F. Y. Gao, X. L. Zhang, P. P. Yang, R. Liu, L. P. Chi, Z. Z. Wu, S. Qin, X. X. Yu and M. R. Gao, *J. Am. Chem. Soc.*, 2021, **143**, 8011–8021.

43 W. L. Zhu, Y. J. Zhang, H. Y. Zhang, H. F. Lv, Q. Li and S. H. Sun, *J. Am. Chem. Soc.*, 2014, **136**, 16132–16135.

44 W. L. Zhu, R. Michalsky, H. F. Lv, X. L. Sun, A. A. Peterson and S. H. Sun, *J. Am. Chem. Soc.*, 2013, **135**, 16833–16836.

45 S. Back, M. S. Yeom and Y. S. Jung, *ACS Catal.*, 2015, **5**, 5089–5096.

46 D. S. Chen, W. B. Yu, Z. Deng, J. Liu, J. Y. Jin, M. Wu, L. H. Chen and B. L. Su, *RSC Adv.*, 2015, **5**, 55520–55526.

47 T. T. Zhao, J. H. Li, J. D. Liu, F. M. Liu, K. Q. Xu, M. Yu, W. Xu and F. Y. Cheng, *ACS Catal.*, 2023, **13**, 4444–4453.

48 A. Xu, S. F. Hung, A. Cao, Z. Wang, N. Karmodak, J. E. Huang, Y. Yan, A. Sedighian Rasouli, A. Ozden, F. Y. Wu, Z. Y. Lin, H. J. Tsai, T. J. Lee, F. Li, M. Luo, Y. Wang, X. Wang, J. Abed, Z. Wang, D. H. Nam, Y. C. Li, A. H. Ip, D. Sinton, C. Dong and E. H. Sargent, *Nat. Catal.*, 2022, **5**, 1081–1088.

49 S. Jiang, K. Klingan, C. Pasquini and H. Dau, *J. Chem. Phys.*, 2019, **150**, 041718.



50 M. W. Fang, M. L. Wang, Z. W. Wang, Z. X. Zhang, H. C. Zhou, L. M. Dai, Y. Zhu and L. Jiang, *J. Am. Chem. Soc.*, 2023, **145**, 11323–11332.

51 X. Y. Chen, D. A. Henckel, U. O. Nwabara, Y. Y. Li, A. I. Frenkel, T. T. Fister, P. J. A. Kenis and A. A. Gewirth, *ACS Catal.*, 2020, **10**, 672–682.

52 W. Zhang, C. Huang, Q. Xiao, L. Yu, L. Shuai, P. An, J. Zhang, M. Qiu, Z. Ren and Y. Yu, *J. Am. Chem. Soc.*, 2020, **142**, 11417–11427.

53 G.-Y. Duan, X.-Q. Li, G.-R. Ding, L.-J. Han, B.-H. Xu and S.-J. Zhang, *Angew. Chem., Int. Ed.*, 2022, **61**, e202110657.

54 F. Li, Y. C. Li, Z. Wang, J. Li, D.-H. Nam, Y. Lum, M. Luo, X. Wang, A. Ozden, S.-F. Hung, B. Chen, Y. Wang, J. Wicks, Y. Xu, Y. Li, C. M. Gabardo, C.-T. Dinh, Y. Wang, T.-T. Zhuang, D. Sinton and E. H. Sargent, *Nat. Catal.*, 2020, **3**, 75–82.

55 A. Singhal, M. R. Pai, R. Rao, K. T. Pillai, I. Lieberwirth and A. K. Tyagi, *Eur. J. Inorg. Chem.*, 2013, **14**, 2640–2651.

56 M. Zheng, P. Wang, X. Zhi, K. Yang, Y. Jiao, J. Duan, Y. Zheng and S.-Z. Qiao, *J. Am. Chem. Soc.*, 2022, **144**, 14936–14944.

57 I. V. Chernyshova, P. Somasundaran and S. Ponnurangam, *Proc. Natl. Acad. Sci. U.S.A.*, 2018, **115**, E9261–E9270.

58 X. Wang, P. Ou, A. Ozden, S.-F. Hung, J. Tam, C. M. Gabardo, J. Y. Howe, J. Sisler, K. Bertens, F. P. G. de Arquer, R. K. Miao, C. P. O'Brien, Z. Wang, J. Abed, A. S. Rasouli, M. Sun, A. H. Ip, D. Sinton and E. H. Sargent, *Nat. Energy*, 2022, **7**, 170–176.

59 F. Li, A. Thevenon, A. Rossas-Hernández, Z. Wang, Y. Li, C. M. Gabardo, A. Ozden, C. T. Dinh, J. Li, Y. Wang, J. P. Edwards, Y. Xu, C. McCallum, L. Tao, Z.-Q. Liang, M. Luo, X. Wang, H. Li, C. P. O'Brien, C.-S. Tan, D.-H. Nam, R. Quintero-Bermudez, T.-T. Zhuang, Y. C. Li, Z. Han, R. D. Britt, D. Sinton, T. Agapie, J. C. Peters and E. H. Sargent, *Nature*, 2020, **577**, 509–513.

60 H. Y. An, L. F. Wu, L. D. B. Mandemaker, S. Yang, J. de Ruiter, J. H. J. Wijten, J. C. L. Janssens, T. Hartman and B. M. Weckhuysen, *Angew. Chem., Int. Ed.*, 2021, **60**, 16576–16584.

61 Y. W. Jiang, X. Y. Wang, D. L. Duan, C. H. He, J. Ma, W. Q. Zhang, H. J. Liu, R. Long, Z. B. Li, T. T. Kong, X. J. Loh, L. Song, E. Y. Ye and Y. J. Xiong, *Adv. Sci.*, 2022, **9**, 2105292.

62 F. Q. Yu, X. Liu, L. L. Liao, G. M. Xia and H. M. Wang, *Small*, 2023, 2301558.

63 C. Liu, M. M. Wang, J. Y. Ye, L. B. Liu, L. G. Li, Y. H. Li and X. Q. Huang, *Nano Lett.*, 2023, **23**, 1474–1480.

64 M. Liu, Q. Y. Wang, T. Luo, M. Herran, X. Y. Cao, W. R. Liao, L. Zhu, H. M. Li, A. Stefancu, Y.-R. Lu, T.-S. Chan, E. Pensa, C. Ma, S. G. Zhang, R. Y. Xiao and E. Cortés, *J. Am. Chem. Soc.*, 2024, **146**, 468–475.

65 S. Q. Zhu, T. H. Li, W.-B. Cai and M. H. Shao, *ACS Energy Lett.*, 2019, **4**, 682–689.

66 S. H. Min, X. Xu, J. X. He, M. Sun, W. L. Lin and L. T. Kang, *Small*, 2024, 2400592, DOI: [10.1002/smll.202400592](https://doi.org/10.1002/smll.202400592).

67 Y. Zheng, A. Vasileff, X. Zhou, Y. Jiao, M. Jaroniec and S. Z. Qiao, *J. Am. Chem. Soc.*, 2019, **141**, 7646–7659.

68 Y. Kim, S. Park, S.-J. Shin, W. Choi, B. K. Min, H. Kim, W. Kim and Y. J. Hwang, *Energy Environ. Sci.*, 2020, **13**, 4301–4311.

69 H. Luo, B. Li, J. G. Ma and P. Cheng, *Angew. Chem., Int. Ed.*, 2022, **61**, e202116736.

70 J. Q. Feng, L. M. Wu, S. J. Liu, L. Xu, X. N. Song, L. B. Zhang, Q. G. Zhu, X. C. Kang, X. F. Sun and B. X. Han, *J. Am. Chem. Soc.*, 2023, **145**, 9857–9866.

71 W. C. Ma, S. J. Xie, T. T. Liu, Q. Y. Fan, J. Y. Ye, F. F. Sun, Z. Jiang, Q. H. Zhang, J. Cheng and Y. Wang, *Nat. Catal.*, 2020, **3**, 478–487.

72 Z. M. Wei, J. Ding, X. X. Duan, G.-L. Chen, F.-Y. Wu, L. Zhang, X. J. Yang, Q. Zhang, Q. Y. He, Z. Y. Chen, J. Huang, S.-F. Hung, X. Yang and Y. M. Zhai, *ACS Catal.*, 2023, **13**, 4711–4718.

